Applied Clay Science 233 (2023) 106827

Contents lists available at ScienceDirect

Applied Clay Science

journal homepage: www.elsevier.com/locate/clay

Research Paper

Modified halloysite nanotubes decorated with Ceria for synergistic corrosion inhibition of Polyolefin based smart composite coatings

Ahmadyar Qureshi [a,b,1], Sehrish Habib [a,c,1], Muddasir Nawaz [a], R.A. Shakoor [a,c,*], Ramazan Kahraman [d], Elsadig Mahdi Ahmed [c,**]

[a] Center for Advanced Materials (CAM), Qatar University, 2713 Doha, Qatar
[b] College of Arts and Sciences, Qatar University, 2713 Doha, Qatar
[c] Department of Mechanical and Industrial Engineering, Qatar University, 2713 Doha, Qatar
[d] Department of Chemical Engineering, Qatar University, 2713 Doha, Qatar

ARTICLE INFO

Keywords:
Halloysite nanotube
Sodium dodecyl sulfate
Ceria
Polyolefin coating
Corrosion inhibition

ABSTRACT

The deteriorating effect of corrosion can be controlled by applying suitable polymeric-based coatings. In this work, polyolefin based smart composite coatings containing modified halloysite nanotubes decorated with ceria particles were investigated to analyze their anti-corrosion behavior. For this purpose, halloysite nanotubes (Hals) were utilized as nanocarriers which were loaded with sodium dodecyl sulfate (SDS) as a corrosion inhibitor via overnight stirring and vacuum cycling method. The loaded Hals were then modified/decorated with cerium oxide (CeO_2) particles by reacting cerium nitrate ($Ce(NO_3)_3.6H_2O$) and sodium hydroxide (NaOH) which resulted in the formation of CeO_2@HAL/SDS. The synthesized modified particles (CeO_2@HAL/SDS) were characterized by energy-dispersive X-ray spectroscopy (EDX), Transmission electron microscopy (TEM), Fourier-Transform Infrared Spectrometer (FTIR), Thermogravimetric analysis (TGA), and differential thermal gravimetric analysis (DTA), X-ray diffraction analysis (XRD) and UV–vis spectroscopic analysis. TGA analysis results demonstrated that about 32% (*w*/w) of SDS has been loaded into Hal, and 47% (w/w) of CeO_2 has been immobilized on the surface of Hal. UV–Vis analysis results demonstrated the pH-sensitive and time-dependent release behavior of synthesized particles. Furthermore, the modified CeO_2@HAL/SDS particles (1 wt%) were reinforced into the polyolefin-based matrix, coated on a polished steel substrate and their electrochemical properties were investigated. The electrochemical impedance spectroscopy (EIS) analysis confirms the promising improvement in the corrosion inhibition performance of polyolefin coatings modified with CeO_2@HAL/SDS particles when compared to the polyolefin composite coatings modified with HAL/SDS due to the synergistic corrosion inhibition performance of $Ce(OH)_3$ and Fe-SDS formation at the cathodic and anodic region of steel.

1. Introduction

Corrosion is detrimental to industrial equipment damage and failure, turning it into one of the biggest challenges for manufacturers worldwide. Protection against corrosion is almost all industrialists' topmost priority regarding operational processes' feasibility and efficiency (Koch, 2017). Therefore, a long-term solution of prevention against corrosion is required. There have been multiple studies on the best ways to minimize damages incurred due to corrosion, and the results have been explained vastly (Hinton, 2022). These protective methods include using corrosion-resistant materials, altering environmental conditions, regularly replacing equipment, etc. However, protective coatings have caught the attention of scientists worldwide and have proven to be the most economical and efficient form of corrosion defense (Montemor, 2014).

Protective coatings are applied over equipment and pipelines to reduce corrosion by acting as a line of defense against various kinds of mechanical and physical damage, including scratches and erosion (Stankiewicz et al., 2013). The direct addition of an inhibitor is not a good idea as it may interact with the matrix and lead to extreme

* Corresponding author at: Center for Advanced Materials (CAM), Qatar University, 2713 Doha, Qatar.
** Corresponding author.
E-mail addresses: shakoor@qu.edu.qa (R.A. Shakoor), elsadig@qu.edu.qa (E.M. Ahmed).
[1] Authors with equal contributions.

https://doi.org/10.1016/j.clay.2023.106827
Received 17 October 2022; Received in revised form 20 December 2022; Accepted 19 January 2023
Available online 25 January 2023

reactions rendering the coating useless (Kamburova et al., 2018). Therefore, to avoid this issue, the inhibitor is encapsulated into a nanocontainer which releases upon a change in its environment. The mechanism of anti-corrosion coatings has been discussed in detail numerous times (Ding et al., 2018). Studies have explained various ways in which these coatings work; they may form a barrier between the environment and the material to be protected, inhibit the process of corrosion itself, or act in a way that the coating gets corroded instead of the material to which it is applied (sacrificial coatings).

Nanocontainers have been used to encapsulate various functional species and develop various self-healing coatings. The inhibitors added in these containers are usually triggered by external stimulus or pH changes; this type of trigger makes the coatings durable over long periods as none of the inhibitors seeps/leaks out unless required (Grigoriev et al., 2017). Moreover, hybrid nanocontainers have been significantly studied in recent years due to their increased loading capacity and longer-lasting protection (Amiri and Rahimi, 2014). These nanocontainers are impregnated with a corrosion inhibitor released in response to the change in pH caused by the corrosion process.

A new material known as halloysite nanotube (Hal) has been on the rise in research and development owing to its impressive characteristics, including nanoscale lumens, low surface (hydr)oxides group density, and low cost. These properties and their nano size allow Hal to be utilized in numerous applications in various (Du et al., 2010; Kamble et al., 2012; Yuan et al., 2015; Pandey et al., 2017, 2022b; Pandey et al., 2022a; Rawtani et al., 2017; Tharmavaram et al., 2018, 2021) Hal has also shown promising results when used for smart corrosion coatings where the inhibitors are embedded into these containers and released at a higher and more controlled rate than regular direct coatings, preventing the rapid spread of corrosion in corrosive environments (Zahidah et al., 2017).

The unique properties, porous structure, and small size of Hals enable them to be used for controlled drug delivery purposes. These nanotubes have also been frequently used for carrying inhibitors and as reinforcement in corrosion-protective polymeric composite coatings (Deepak and Agrawal, 2012; Tharmavaram et al., 2023). Moreover, Hals have also been used for cement-based coatings. One such work was established by Monica Tonelli et al. when they prepared these cementitious coatings using Hal, nano silica, and benzotriazole. UV–vis spectroscopy showed the release of BTA, and it was found that Hal can also be used for delivering anti-corrosion molecules for cement mortars (Tonelli et al., 2020). Yuanwei Liu et al. (Liu et al., 2022a) encapsulated Hal with benzotriazole (BTA) as a corrosion inhibitor by employing layer by layer technique to study the corrosion inhibition performance of poly epoxy-based composite coatings. The results demonstrated the controlled release of BTA due to the change in pH and temperature. Electrochemical impedance spectroscopy analysis demonstrated the decent corrosion inhibition performance of poly epoxy-based composite coatings. Yanli Zhang et al. (Zhang et al., 2022a) loaded sodium D-gluconate (SD) into Hal. The lumen of Hal was extended by etching it at various concentrations of sulfuric acid (H_2SO_4) and sodium hydroxide (NaOH). Chitosan (CS) and Sodium alginate (SA) was incorporated to synthesize SD-Hal-A3@CS/SA. The synthesized nanocontainer was reinforced into epoxy-based coatings to study the corrosion inhibition performance of coatings. The EIS results demonstrated the good corrosion inhibition performance of modified coatings.

In this work we modified Hal by loading corrosion inhibitor (SDS) into them and then immobilized the ceria nanoparticle on the surface of modified Hal. The synthesized particles were reinforced into polyolefin-based matrix followed by its coating on steel substrate to study the corrosion inhibition performance of modified coatings. Various characterization techniques were employed to study the morphological, chemical interaction and thermal stability studies of the synthesized particles. EIS analysis was done to study the corrosion protection behavior of the modified polyolefin based smart composite coatings. The results obtained from EIS demonstrated that the modified coatings displayed improved corrosion inhibition performance in 3.5 wt% NaCl solution.

2. Experimental

2.1. Chemicals used

Halloysite nanotubes (Hals) are used as the carrier, Sodium dodecyl sulfate (SDS) is used as a corrosion inhibitor, Cerium nitrate Ce $(NO_3)_3.6H_2O$, Absolute Ethanol, Sodium Hydroxide pellets, Hexamethylene tetramine (HMT), Hydrogen peroxide (H_2O_2), Sodium chloride (NaCl) were bought from Sigma Aldrich and were utilized as received. Dow chemical provided CANVERA™ 1110 Polyolefin, which was utilized as a polymeric matrix. A local supplier provided Carbon steel coupons ($35 \times 35 \times 1$ mm^3) which were utilized as substrates (with composition of C = 0.21%, P = 0.30%, S = 0.04%, Cu = 0.20% and Fe = balanced and thickness of 1 mm). For the polishing of steel substrates, silicon carbide abrasive was procured from Hebei Yineng pipeline Group Co., Ltd., China.

2.2. Loading of Hal with SDS as a corrosion inhibitor

The loading of SDS into pristine Hal followed the same procedure as discussed (Habib et al., 2019, 2020b). Following this, 4 g of SDS was dissolved in the 25 mL of respective solvent (distilled water) to form a saturated solution. 2 g of Hal were then added into the saturated solution of SDS. This solution was then kept for overnight stirring at 700 rpm at room temperature (25 °C). After stirring, the same solution was placed under vacuum cycling for 4 h to remove excess entrapped air in Hal. This step will ensure that the maximum amount of SDS will be loaded into Hal (Dyab et al., 2018; Izadi et al., 2019; Jia et al., 2020; Zhang et al., 2022b). After 4 h, the solution underwent centrifugation at 5000 rpm for 15 min. This resulted in separating the resultant product (HAL/SDS). The product was then dried in the oven at 60 °C for 24 h. After 24 h, the dried product was grounded in a mortar and pestle to get fine particles. The schematic of the procedure is represented in Fig. 1.

2.3. Immobilization of CeO_2 on HAL/SDS

The schematic for the synthesis of CeO_2@HAL/SDS is represented in Fig. 1. The synthesis of CeO_2@HAL/SDS followed the chemical precipitation method (Habib et al., 2022). For this objective, the 1 g synthesized HAL/SDS particles were added to 2 g of $Ce(NO_3)_3.6H_2O$ and 30 mL of ethanol. The solution was then set for sonication for 30 min. While this solution was on sonication, in another beaker 3.23 g of HMT was added to 20 mL of distilled water. This solution was added to the sonicated solution, followed by proper agitation at 75 °C for 2 h. 40 μL of H_2O_2 was added into this solution while on agitation for the complete oxidation of cerium nitrate to cerium oxide. After 2 h, the resultant precipitates were collected and filtered while rinsing with distilled water. The filtered particles were then dried at 80 °C for 8 h and then calcinated at 500 °C for 2 h in the furnace. This will result in the formation of CeO_2@HAL/SDS particles.

2.4. Steel substrate preparation

Steel coupons obtained from a local company were polished using Metkon ForcoPol IV grinding and polishing machine. Silicon carbide (SiC) abrasive paper (120-2c) was employed to polish coupons. After polishing, the coupons were cleaned with ethanol and properly dried to prevent the formation of the oxide layer and rust on the surface of the coupons.

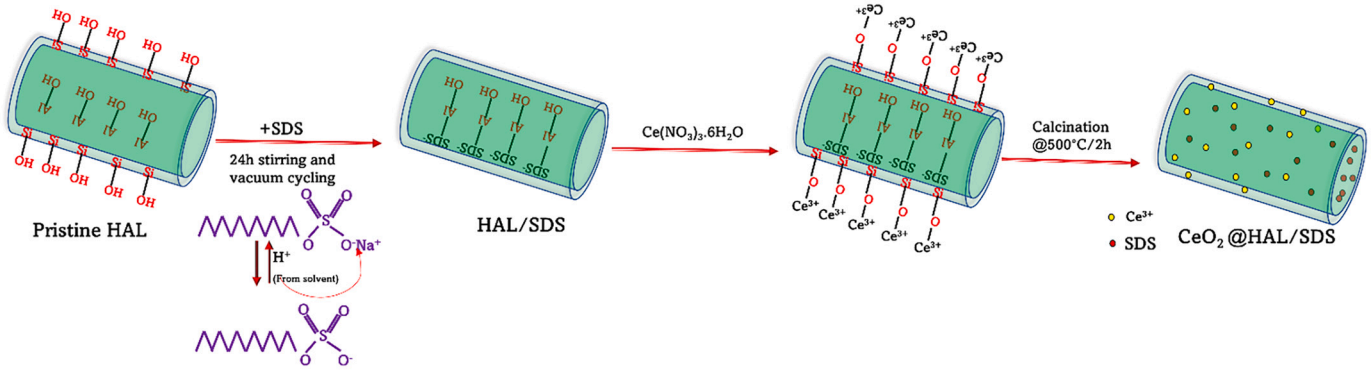

Fig. 1. Schematics for the synthesis of HAL/SDS and CeO_2@HAL/SDS.

2.5. Synthesis of Polyolefin based modified composite coatings and development of smart composite coatings on steel substrate

To synthesize Polyolefin-based modified coating, 1 wt% of HAL/SDS and 1 wt% of CeO_2@HAL/SDS was added into Polyolefin. To make a uniform dispersion, firstly, the modified particles were added to alkaline water (pH ~ 9) to make a paste-like consistency. Then Polyolefin was added slowly with gentle mixing with a glass rod. The solution was then left to stir at 300 rpm for 24 h at room temperature (25 °C). The synthesized coating mixture was then applied over polished steel substrate via dip coating technique (dip cycle = 1, immersion speed = 22 mm/min, and with-drawl speed = 16 mm/min). The coatings were then cured in an oven at a temperature between 70 and 165 °C. The thickness of coatings was measured by employing PosiTector 6000 from DeFelsko (Made in the USA), and it came out to be 70 μm. Reference or blank polyolefin coatings were not synthesized as they were already cited in our previous work (Habib et al., 2022). Two forms of coatings were synthesized. One with HAL/SDS labeled as PO-HAL/SDS and the other with CeO_2@HAL/SDS labeled as PO- CeO_2@HAL/SDS.

2.6. Characterization of synthesized modified particles and Polyolefin based smart composite coatings

The synthesized modified particles (HAL/SDS and CeO_2@HAL/SDS) were characterized by employing energy-dispersive X-ray spectroscopy (EDX), Transmission electron microscopy (TEM), Frontier Transform Infrared spectrometer (FTIR), Thermogravimetric analysis (TGA) and differential thermal gravimetric analysis (DTA), X-ray diffraction analysis (XRD)and UV–vis spectroscopic analysis. To analyze the self-healing behavior or corrosion inhibition performance Electrochemical Impedance Spectroscopy (EIS) analysis was employed over 30 days in 3.5 wt% NaCl solution. The detailed specifications of all the techniques are mentioned in our previous work (Habib et al., 2022).

3. Results and discussions

3.1. Structural and morphological analysis

FTIR analysis was done to analyze the chemical bonding between the different synthesized particles, as represented in Fig. 2. The FTIR spectra for Pristine Hal, HAL/SDS, and CeO_2@HAL/SDS were recorded within the range of 4000–500 cm^{-1}. The successful modification and functionalization of Hal were determined by observing various interactions between functional groups of synthesized particles. In the case of the pristine Hal, the characteristics bands appeared at 3695, 3621, 1646, 1123, 996, 902, and 746 cm^{-1}. These bands represent the O-H stretching of the (hydr)oxides group present in the inner surface related to the Al-OH stretching, Si-O-Si deformation, and Si-O and O-H group deformation stretching of the outer (hydr)oxides group, respectively (Asadi et al., 2019; Barman et al., 2020; Chen et al., 2020). After modifying Hal with SDS, we can see slight displacement in the bands of the Hal which is an indication of the interaction of SDS with Hal. Along with the displaced characteristic bands of Hal, the characteristics bands of SDS can also be observed in FTIR spectra of HAL/SDS at 2955, 2912, 2847, 1464, 1213, 1079 and 827 cm^{-1}. The bands at 2955, 2912, and 2847 cm^{-1} are related to the CH_2 stretching and bending vibrations bands. The band at 1464 corresponds to the C-H symmetric stretching vibrations. The band at 1213 cm^{-1} is related to the skeleton vibration due to the stretching of the bridge S-O bond. The band at 1079 and 827 cm^{-1} is attributed to the C-C bond stretching and asymmetric C-H bending of the CH_2 group of SDS (Pasbakhsh et al., 2010; Singh et al., 2011; Lun et al., 2014). The appearance of the distinctive bands of the SDS is evidence of the successful modification of Hal with SDS. The FTIR spectra of CeO_2@HAL/SDS also represented the characteristics band of Hal with slight displacement, again demonstrating the chemical interaction between synthesized particles. Some of the characteristic bands of SDS are also observed in CeO_2@HAL/SDS spectra. The bands of ceria are observed around 597 cm^{-1}, which represents the metal oxide stretching vibration bands (Habib et al., 2020a). The presence of the distinguished bands of the Hal and ceria is a validation of the interaction between these two. The displacement in the peaks of Hal is due to the disturbance of the structure of the Hal due to the additional chemical bonding between ceria and Hal.

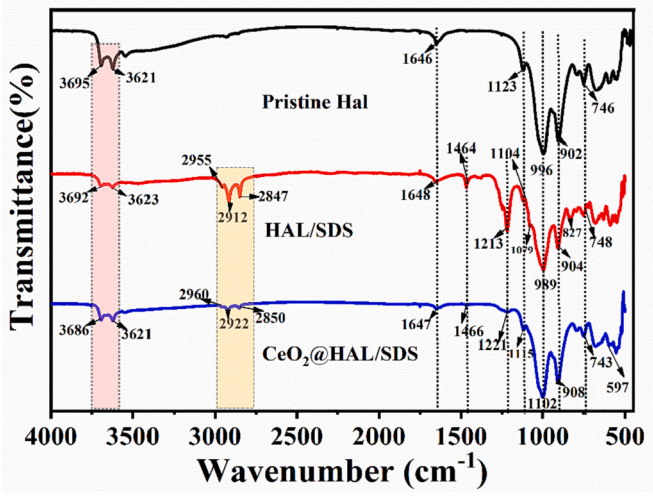

Fig. 2. FTIR analysis of the pristine Hal, HAL/SDS, and CeO_2@HAL/SDS.

The morphology of pristine Hal, HAL/SDS, and CeO_2@HAL/SDS was analyzed by TEM and endorsed by EDX analysis, as shown in Fig. 3. Hal represents the tubular structure with an empty lumen and smooth surface (Fig. 3a). Hal is composed of an outer silica layer (Si-O-Si group)

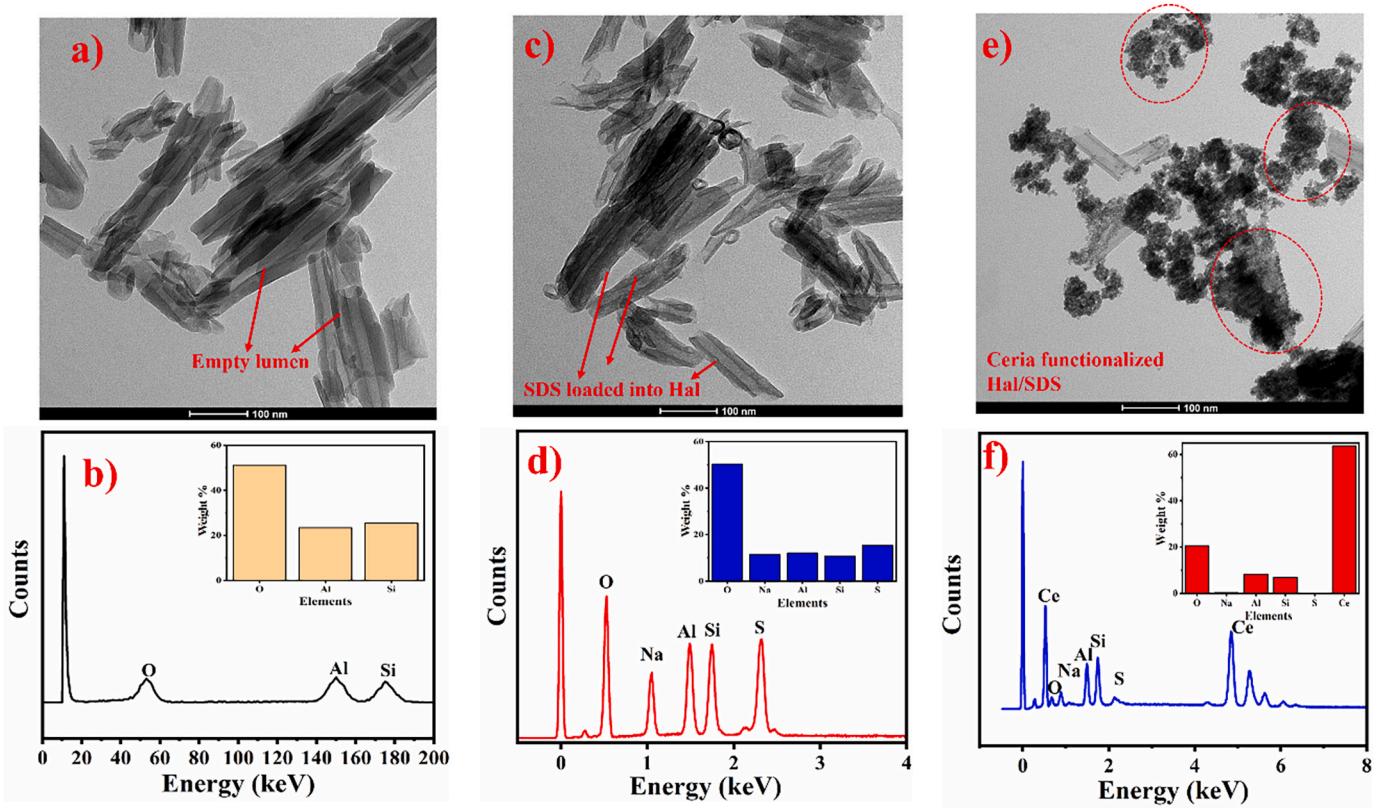

Fig. 3. TEM and EDX analysis of (a, b) Pristine Hal, (c, d) HAL/SDS, and (e, f) CeO_2@HAL/SDS.

and inner alumina (Al-OH) layer with a chemical formula of $Al_2Si_2(OH)_4.nH_2O$. The hollow tubular structure of Hal is because of the strain caused by lattice mismatch between the oxygen-sharing alumina and silica layer (Yurdacan and Murat Sari, 2021). The EDX analysis results (Fig. 3b) demonstrated that Hal is mainly composed of Al, Si, and oxygen with weight percentages of 23.41, 25.41, and 51.18%, respectively. After the loading of SDS into Hal, the TEM analysis results (Fig. 3c) represented that the apparent morphology of Hal remained unchanged. However, SDS particles can be seen inside the Hal structure. Most of the loading of SDS is seen in the outer layer of Hal. The EDX results (Fig. 3d) demonstrated that apart from the main elements of Hal (Al, Si), the main elements of SDS also appeared, which are Na and S, which is evidence of the presence of SDS in Hal (Lun et al., 2014). The weight percentages of the respective elements are O = 50.34, Na, 11.41, Al = 12.12, Si = 10.78, and S = 15.34. The TEM analysis results of CeO_2@HAL/SDS (Fig. 3e) represent the formation of CeO_2 on Hal. It is attributed to the adsorption of the ceria molecules on the outer layer of the Hal due to the hydrogen bonding between ceria and Hal. Ceria particles appeared spherical in structure and unevenly distributed on the outer surface of Hal. The outer surface usually has defects which makes Hal accessible for modification (Jana et al., 2015). This suggests that the cerium nitrate particles are converted to CeO_2 by the interaction with Hal in the presence of HMT and H_2O_2 as shown in the schematic illustration Fig. 1. The EDX analysis results (Fig. 3f) revealed that the appearance of Ce is evidence of the formation of Ceria on the outer layer of Hal. The weight percentage of ceria is 63.66% which is contributed to the main weight percentage of the synthesized product. The decrease in the weight percentage of the Al, Si, Na, and S (8.3, 7, 0.32, and 0.11), respectively, is also evidence that Ceria has covered the outer surface of the Hal.

Based on the weight percentages data obtained from EDX analysis, the ratio of Al/Si for the pristine Hal is 1.18, which is decreased to 1.13 for the HAL/SDS and 1.08 for the CeO_2@HAL/SDS. The decrease in the ratio of the Al/Si of the pristine Hal could appear due to the incorporation of SDS into the interlayers of Hal in the case of HAL/SDS. There is the possibility of the ion exchange between Na^+ of SDS and Al $(OH)_2^-$ of Hal. Similarly, in the case of CeO_2@HAL/SDS, the decrease is observed due to the interaction of Cerium ions with Si of the Hal in the outer layer. Cerium ions take the major composition of the pristine Hal, as shown in the EDX of CeO_2@HAL/SDS (Fig. 3f).

The diffraction pattern of the Pristine Hal, HAL/SDS, and CeO_2@HAL/SDS was analyzed by the XRD technique, as represented in supplementary fig. S1. The pristine Hal is representing the characteristic reflection at 2θ of 11.69°, 19.94°, 24.74°, 34.96°, 54.85°, and 62.40°. The diffraction planes associated with the corresponding 2θ are (001), (100), (002), (110), (210), and (300), respectively complementing the JCPDS card # 98–018-6723. In the case of the XRD pattern of HAL/SDS, no new reflection is seen, indicating that SDS intercalation didn't change the morphology of Hal as observed in TEM images. However, the displacement in the reflection is seen, which is evidence of the interaction of SDS with Hal. It has also been observed that the peak reflected at 2θ = 11.69° (001) didn't shift to lower values, which indicates that SDS is not intercalated to the interlayer of Hal but only in the outer layer. This is because most of the (hydr)oxides groups in interlayers are embedded and are not available for loading SDS into Hal (Jana et al., 2015). In the case of CeO_2@HAL/SDS, most of the peak's intensity is weakened, and some disappear, which may be due to the deposition of the ceria on Hal and the high-temperature calcination process (Zhang et al., 2015). One peak splitting is seen at 2θ = 27.5° and 28.6°, indicating the formation of a new phase. The peak at 2θ = 28.6° corresponds to the (111) diffraction plane of CeO_2 (Habib et al., 2022).

3.2. *Thermal stability analysis of synthesized particles*

The thermogravimetric (TGA) and differential thermal analysis (DTA) of Pristine Hal, HAL/SDS, and CeO_2@HAL/SDS are represented in Figs. 4(a, b). Pristine Hal represented mass loss in four stages. In the first stage, Hal experienced a mass loss of 2% due to water in the

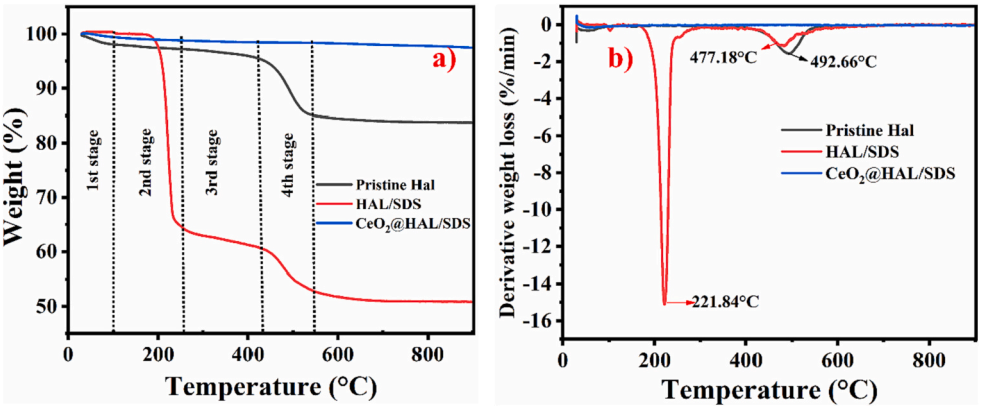

Fig. 4. TGA (a) and DTA (b) analysis of Pristine Hal, HAL/SDS, and CeO_2@HAL/SDS.

structure or interlayer water contents. In the second stage, the mass loss is almost constant until the end of the third stage. Till the third stage, Hal encountered a total of 5% mass loss only, which is considered as water mass loss. The major mass loss is seen in the fourth stage at around 492 °C. Almost a total of 15% mass loss is seen in this stage. This mass loss is due to the de(hydr)oxidization of the Al-OH group of Hal and the development of meta halloysite. After this stage, the mass loss is constant. No further mass loss is seen after the fifth stage. If we investigate the DTA curve of the pristine Hal, similar behavior has been observed. In the first stage, the first small endothermic peak is seen at around 50 °C, which is water mass loss as seen in the TGA curve. The structural decomposition of Hal is seen at around 492.66 °C due to the de(hydr) oxidization of Hal, as explained earlier in this section (Heraiz et al., 2017).

In the case of HAL/SDS, mass loss is observed to be constant in the first stage showing that SDS does not contain any free water molecules and the product was completely dried. The huge mass loss occurs in the second stage between 174 and 254 °C. This mass loss is due to the degradation of SDS. This huge mass loss is entailed by the breakdown of long alkyl chains of SDS (Lun et al., 2014). Almost 35% of mass loss is seen in this stage. In the third stage, only 4% mass loss was observed, but it continued to decrease until the fourth stage when we noted the degradation of Hal at 477 °C. The residual mass loss at 890 °C for pristine Hal and HAL/SDS indicated that 32% of SDS has been loaded into Hal. In the DTA curve of HAL/SDS, two endothermic peaks have been observed at 221 and 477 °C, demonstrating the decomposition of SDS and Hal. In the case of CeO_2@HAL/SDS, no huge mass loss is seen, demonstrating that ceria has covered the Hal (as seen in TEM analysis) so well that the product becomes stable even at high temperatures. The residual mass of CeO_2 and HAL/SDS at 890 °C demonstrated that almost 47% of CeO_2 has been immobilized on the surface of modified Hal (Xie et al., 2011; Chen et al., 2019). Similar behavior has been observed in the DTA analysis of CeO_2@HAL/SDS.

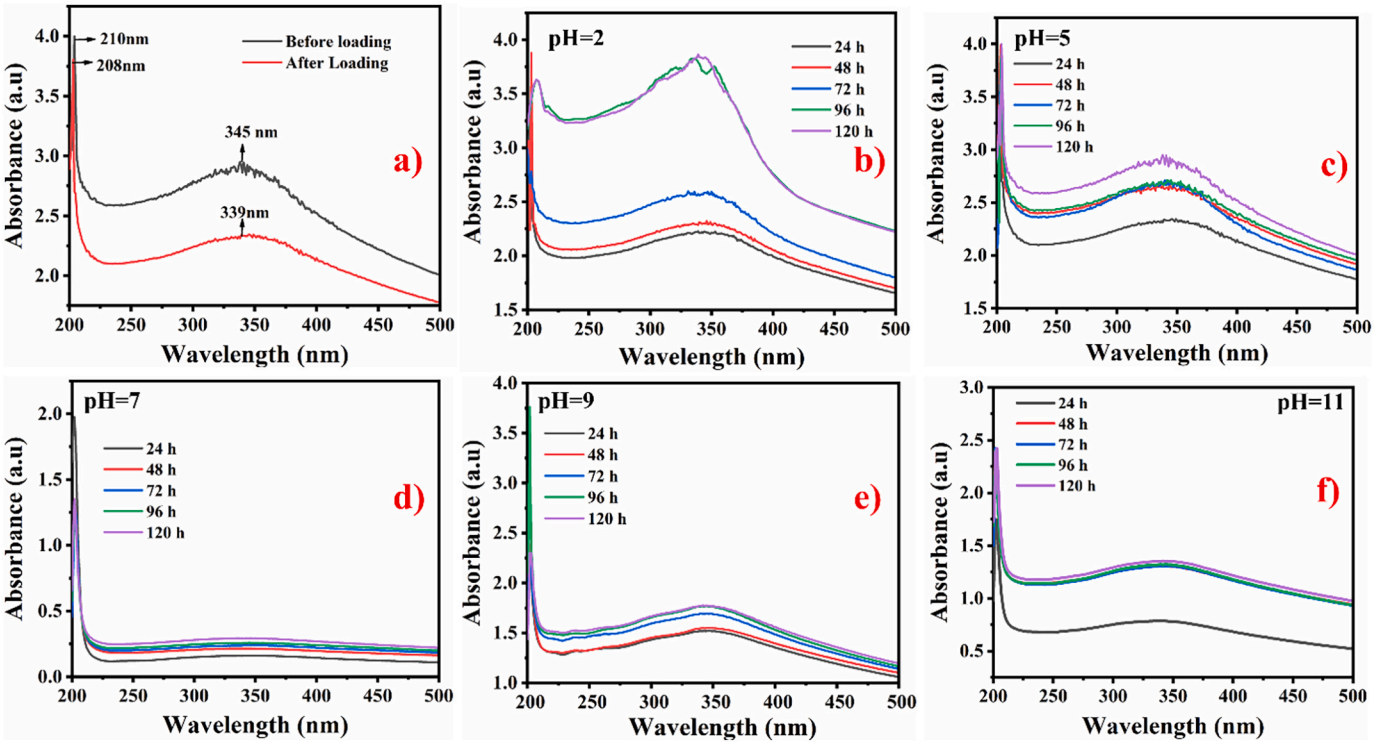

Fig. 5. UV–Vis spectroscopic analysis of a) SDS particles before and after loading into Hal, b, c, d, e, f) CeO_2@HAL/SDS particles at various pH (2, 5, 7, 9, 11) and different time periods (24, 48, 72, 96 and 120 h) respectively, of immersion in 3.5 wt% NaCl solution.

3.3. UV–Vis spectroscopic analysis of synthesized particles

UV–Vis spectroscopic analysis was done to study the pH-sensitive and time-dependent release behavior of the synthesized particles. Fig. 5a demonstrates the UV–vis spectra of SDS before and after loading into Hal. For this purpose, pristine SDS particles and loaded SDS particles were dispersed into 3.5 wt% NaCl solution at pH 2 and stirred for 12 h. After 12 h, UV spectra were recorded to study the change in spectra before and after loading. Before loading, the SDS particles display two absorption peaks at 210 and 345 nm. After loading, hipsochromic (blue shift) is observed, and absorption spectra are displayed to 208 and 339 nm. This shift is due to the interaction of SDS with Hal

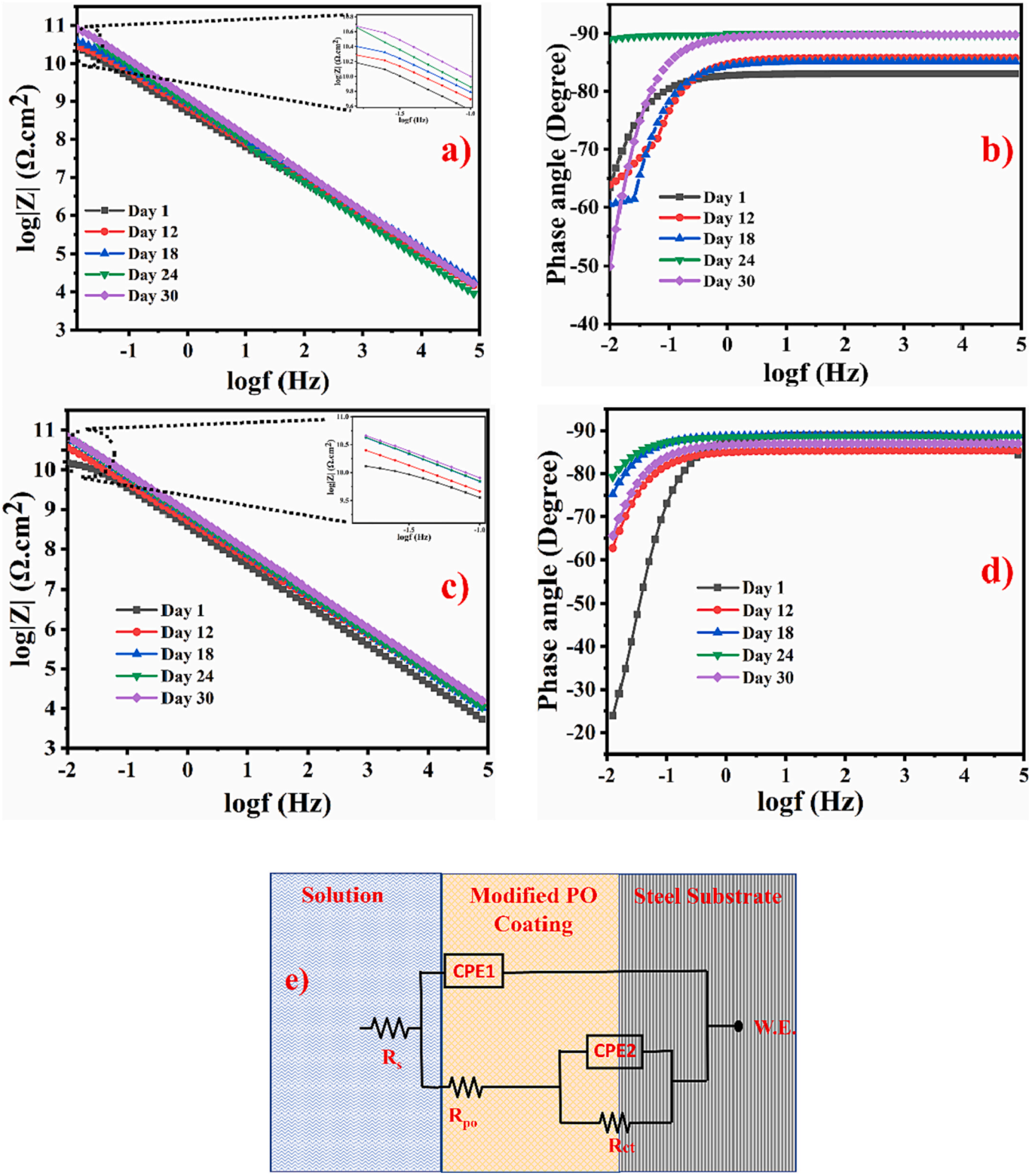

Fig. 6. Bode and Phase angle plots of (a, b) PO-HAL/SDS and (c, d) PO-CeO_2@HAL/SDS coatings (e) Equivalent circuit employed to fit data obtained from EIS analysis of coatings immersed for 30 days in 3.5 wt% NaCl Solution.

while loading. Moreover, the decrease in intensity of particles is also seen in spectra after loading, indicating that particles are less likely available freely in solution as compared to the solution with SDS particles only (Habib et al., 2022).

Fig. 5 (b, c, d, e, f) demonstrates the pH-sensitive and time-dependent release behavior of synthesized particles in 3.5 wt% NaCl solution at various time intervals of 24, 48, 72, 96, 120 h and at different pH (2, 5, 7, 9 11). As shown in the figures, the particles display better release at acidic pH than at basic and neutral pH. The intensity of the absorbance peaks is seen to be more prominent at pH 2 and 5. The appearance of absorption peaks at 210 and 345 nm are due to the π-π* and n-π* transition of an electron in long alkyl chains, respectively. The neutral medium displays less or no release, demonstrating that the particles are not responding to neutral pH. However, particles are released in basic solutions, but the release intensity is less. The prominent release behavior of SDS particles in an acidic medium is also since ceria particles deposited on Hal decompose in an acidic medium, releasing SDS from Hal. Furthermore, the intensity of release of the particles is also seen to be increasing with time, demonstrating that the release behavior of particles is also time dependent.

3.4. Corrosion inhibition performance of developed modified coatings

3.4.1. EIS analysis

EIS analysis was done to study the protective behavior of steel substrate coated with modified polyolefin coatings in 3.5 wt% NaCl solution over 30 days. EIS is one of the effective tools to assess the corrosion inhibition performance of the protective coatings and is a non-destructive technique. The EIS test for each coating was repeated three times to guarantee reproducible results. The corrosion inhibition performance of blank polyolefin coatings (reference coatings) was already cited in our previous work (Habib et al., 2022). The bode and the phase angle plots of the polyolefin coatings were modified with 1 wt% HAL/SDS and CeO_2@HAL/SDS are represented in Fig. 6 after 30 days of immersion in 3.5 wt% NaCl solution. The equivalent circuit employed to fit the obtained data is represented in Fig. 6e. An equivalent circuit with two times constant was developed to fit data of modified coating immersed for 30 days. The different parameters attained after fitting data in EIS analysis are given as R_{po} (Pore resistance), R_{ct} (faradaic resistance), CPE1 (capacitance associated with pore resistance), and CPE2 (double layer capacitance associated with faradic resistance). Due to the deviation of coatings from ideal behavior, constant phase elements (CPE) were employed instead of a capacitor. The values of different parameters obtained from the equivalent circuit are given in table SI (Supplementary data).

The bode and phase angle plot of the reference coatings, as represented in our previous work (Habib et al., 2022), demonstrated the decrease in faradic resistance with time. The phase angle plot also suggested a decrease in the capacitive behavior of the reference coatings. This behavior of the reference coating is attributed to the presence of inherited pores in the coatings. The pores in the coatings lead to the assimilation of electrolytes and form conductive pathways, eventually leading to the deterioration of the coatings with time. The formation of the corrosive species at the metal coating interface eventually leads to the delamination of the coating can be possible.

The bode and phase angle plots of the coatings were modified with 1 wt% HAL/SDS is represented in Fig. 6a. Compared to the reference coatings, the modified coatings displayed exceptional capacitive behavior throughout the frequency range at all immersion times (30 days) in 3.5 wt% NaCl solution. However, at low frequency decrease in capacitive behavior is also seen, but it isn't very important. The bode plot for the PO-HAL/SDS demonstrated an increasing trend in faradic resistance with time. The faradic resistance at low-frequency resistance attained 94.96 $G\Omega.cm^2$ after 30 days of immersion. This value of faradic resistance is higher than that of the reference coatings. This high value of faradic resistance of coatings is associated with a high phase angle of -90° (Fig. 6b). A negligible decrease in phase angle can be associated with interfacial activity but is ignored due to the superior protective behavior of coatings after 30 days of immersion.

The bode and phase angle plot of the polyolefin coatings modified with 1 wt% CeO_2@HAL/SDS are represented in Fig. 6c, d. The trend of the increase in the faradic resistance of these coatings is the same as that of polyolefin coatings modified with HAL/SDS. The faradic resistance demonstrated a notable increase in the corrosion inhibition resistance compared to the reference coatings. The phase angle of the coatings at high frequency is close to -90°. However, for the first days of immersion, the phase angle at low frequency impedance decrease to much lesser value, possibly due to the interfacial activity between the metal and coating interface. For the rest of the days, the decrease in the phase angle is negligible as its above -60°. The coatings are still displaying capacitance behavior. The faradic resistance of the coatings modified with CeO_2@HAL/SDS after 30 days of immersion is observed to be 97.95 $G\Omega.cm^2$. This increased value of faradic resistance compared to the PO-HAL/SDS is due to the synergistic corrosion inhibition effect of corrosion inhibitor (SDS) and cerium hydroxide on the metal surface.

The results of the fitting parameters obtained after fitting data from the equivalent circuit are represented in Fig. 7. The increasing trend of the values of the resistance parameters for both types of coating is observed to be almost the same. Fig. 7a represents the pore resistance of polyolefin coatings modified with 1 wt% HAL/SDS and CeO_2@HAL/SDS. The pore resistance of both types of coatings displayed an increasing trend with high and steady values of 10 $G\Omega.cm^2$. This indicates the high corrosion protective abilities of the modified coatings due to the incorporation of corrosion inhibitors. The pore resistance values of the coatings modified with CeO_2@HAL/SDS are a little higher than those modified with HAL/SDS due to the presence of cerium ions in addition to corrosion inhibitor SDS. This is also evident from the capacitive behavior of the coatings. The decrease in the values of CPE1 (Fig. 7b) and an increase in the Rpo values also endorse the shielding behavior of coatings. These results are evidence of the exceptional protective properties of the modified coatings. In addition to the R_{PO} values, faradic resistance values (R_{ct}) of the coatings obtained from the equivalent circuit after 30 days of immersion are also the coating protection ability, as represented in Fig. 7c. The modified coatings represented a similar increasing trend of values to R_{po}. However, the values of the coatings modified from CeO_2@HAL/SDS are higher than that of HAL/SDS after 30 days of immersion in 3.5 wt% NaCl solution. These increased values of coatings modified from CeO_2@HAL/SDS are due to the synergistic corrosion inhibition of Cerium ions and SDS. The increasing trend in values of R_{ct} is accompanied by a decrease in the values of CPE2, as represented in Table S1. This decrease in the values of CPE2 is an indication of improved corrosion inhibition properties of modified coatings compared to that of reference coatings.

3.4.2. Proposed corrosion inhibition mechanism

The corrosion inhibition mechanism followed by the modified polyolefin coatings is associated with the adsorption of the polar sulfate group of the SDS and cerium ions on a steel substrate. This inhibition is initiated when the electrolyte (3.5 wt% NaCl Solution) interacts with the steel surface. Electrons are transported from the anodic site to the cathodic site. Anode Fe ions are oxidized and interact with a corrosion inhibitor (SDS) to form an inhibitor-iron complex. Due to the reduction process, (hydr)oxides ions will be generated on the cathode, which will interact with cerium ions and form a passive layer. The oxidation and reduction reactions are given by the following equations.

$$Fe \rightarrow Fe^{2+} + 2e^- \text{ (Anodic reaction)} \quad (1)$$

$$Fe^{2+} + SDS \rightarrow Fe^{2+} - SDS \quad (2)$$

$$\frac{1}{2}O_2 + H_2O + 2e^- \rightarrow 2OH^- \text{ (Cathodic reaction)} \quad (3)$$

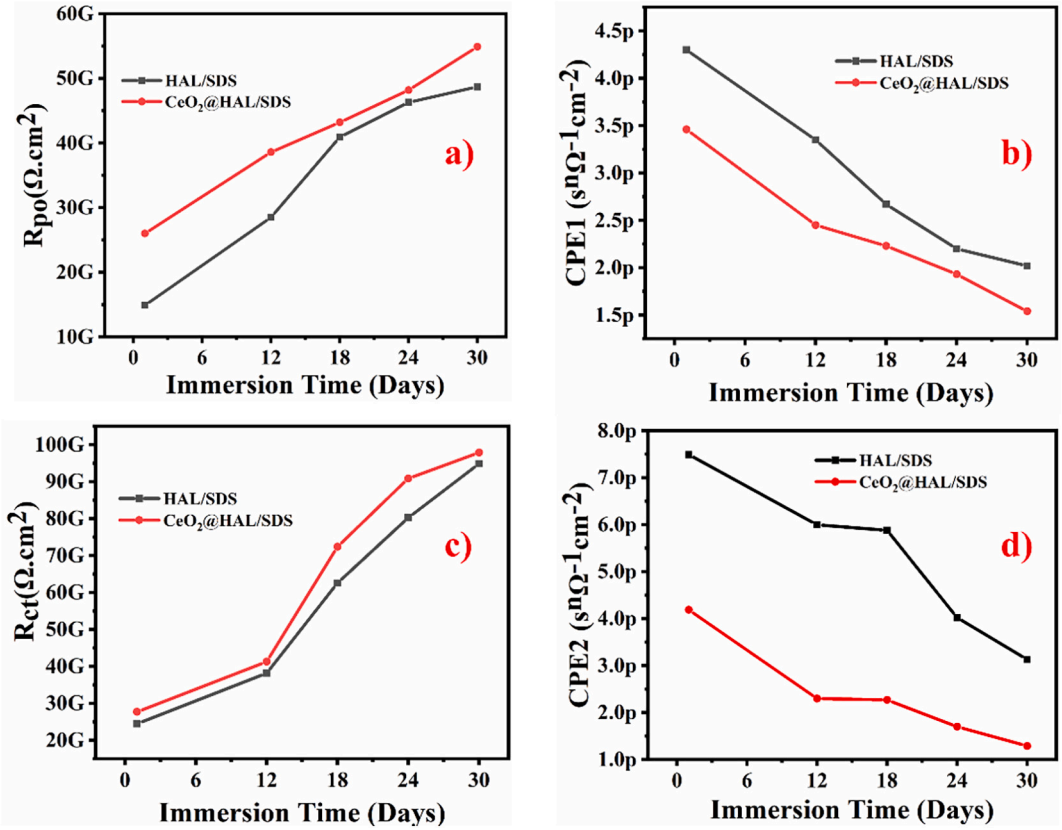

Fig. 7. Evolution of (a) Pore resistance (Rpo), (b) coating capacitance (CPE1), (c) Charge transfer resistance (R_{ct}), and (d) double-layer capacitance (CPE2) in 3.5 wt % NaCl solution over 30 days.

$$Ce^{3+} + 3OH^{-} \rightarrow Ce(OH)_3 \quad (4)$$

The dissociation of the iron is accompanied by the loss of two electrons by the iron in the presence of an electrolyte. Due to the loss of electrons, the iron becomes available with vacant d-orbitals, which then interact with corrosion inhibitors. The release of SDS is already explained in Section 3.3. The released SDS then forms a complex with Fe^{2+} and forms a protective layer at the anodic region. The protection at the cathodic site has related to the release of cerium ions from the outer layers of Hal. Acidic pH facilitates the bond breakage between the Si-O of Hal and CeO_2. Once released, the CeO_2 is dissociated to form cerium ions. The released Ce^{3+} ion then interacts with (hydr)oxides ions at the cathodic site to form $Ce(OH)_3$. So, for the polyolefin coatings modified with CeO_2@HAL/SDS, the steel substrate experienced protection against corrosion due to the synergistic corrosion protection offered by $Ce(OH)_3$ and Fe^{2+}-SDS complex over the entire region of steel. The schematic representing the corrosion inhibition mechanism is also demonstrated in Fig. 8.

A comparison has been done comparing our study with the recently published similar articles to have an overlook of how our work stands different than rest of the recently published articles. For this purpose, a comparison table is added below.

4. Conclusion

In this work, we successfully develop pH-sensitive ceria-modified Hal loaded with SDS to study the synergistic corrosion inhibition performance of polyolefin-based smart coatings. UV–vis analysis results demonstrated that the release of corrosion inhibitor (SDS) was more pronounced in an acidic medium than in a basic or neutral medium. The TGA analysis results demonstrated the good thermal stability of synthesized particles and suggested that 32% (*w*/w) of SDS has been loaded

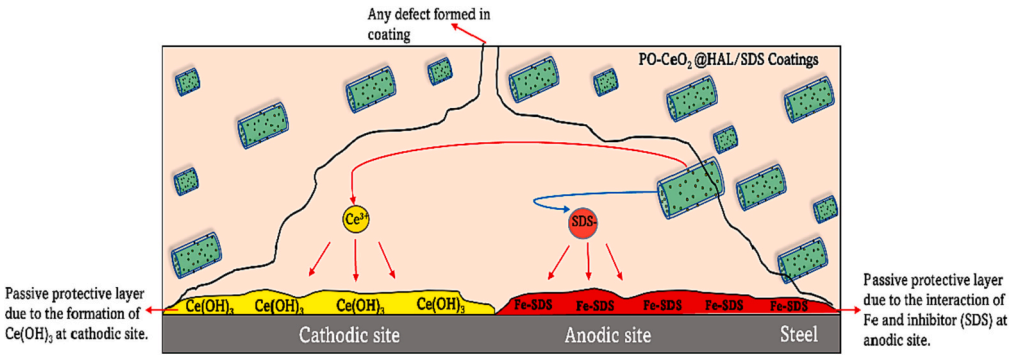

Fig. 8. Schematics of proposed corrosion inhibition mechanism of polyolefin coatings modified with CeO_2@HAL/SDS.

Table 1
Comparison study of corrosion resistance of previously published articles with our study.

Sr no	Coating structure	Corrosion inhibitor	Electrolyte solution	Corrosion Resistance	Ref
1.	Smart epoxy anticorrosion coating based on halloysite nanotubes carrying 8-hydroxy-quinoline on steel	8-hydroxyquinoline	3.5 wt% NaCl solution	1×10^{10} Ω.cm^2	(Liu et al., 2022b)
2.	Capped inhibitor-loaded halloysite nanoclay-based self-healing silica coatings for corrosion protection of mild steel	Benzotriazole	3.5 wt% NaCl	1×10^{6} Ω.cm^2	(Gautam et al., 2022)
3.	Inhibitor-loaded halloysite nanotubes on active corrosion protection of polybenzoxazine coatings on mild steel	Benzotriazole	3.5 wt% NaCl	1×10^{9} Ω.cm^2	(Xu et al., 2019)
4.	L-His@HNTs-rGO provide an integrated anticorrosion for carbon steel	Benzotriazole	3.5 wt% NaCl	1×10^{8} Ω.cm^2	(Jia et al., 2020)
5.	Halloysite Nanotube as Multifunctional Component in Epoxy Protective Coating.	Epoxy loaded HNT	10 wt% NaCl solution	1×10^{9} Ω.cm^2	(Vijayan et al., 2016)
6.	Self-assemble of graphene oxide and polydopamine-coated halloysite nanotubes for enhancing corrosion resistance of waterborne epoxy coating	Benzotriazole (BTA)	3.5 wt% NaCl	1×10^{10} Ω.cm^2	(Chen et al., 2020)

into Hal, and 47% (w/w) of ceria has been immobilized on Hal. TEM and FTIR results suggested the successful loading of SDS in Hal and the immobilization of ceria on the surface of Hal. The reinforcement of 1 wt % of modified smart particles into polyolefin coatings indicated the enhanced active corrosion protection of polyolefin-based smart coatings. The improved corrosion inhibition performance of PO-CeO_2@HAL/SDS coatings compared to the PO-HAL/SDS is attributed to the synergistic corrosion inhibition performance of $Ce(OH)_3$ and FE-SDS on the cathodic and anodic regions respectively of steel substrate. This exceptional corrosion inhibition performance of the developed modified smart polyolefin coatings makes them an attractive candidate for industrial application for the protection of steel.

Author contribution

Conceptualization: Sehrish Habib; Methodology: Sehrish Habib; Software: Sehrish Habib and Ahmadyar Qureshi; Validation: Sehrish Habib and Ahmadyar Qureshi; Formal analysis: Sehrish Habib and Ahmadyar Qureshi; Investigation: Sehrish Habib and Ahmadyar Qureshi; Resources: Abdul Shakoor, Ramazan Kahraman; Data curation: Sehrish Habib and Ahmadyar Qureshi; Writing - original draft: Sehrish Habib and Ahmadyar Qureshi; Writing - review & editing: Sehrish Habib, Muddasir Nawaz, and Abdul Shakoor; Visualization: Sehrish Habib.; Supervision: Elsadig Mahdi Ahmed, Abdul Shakoor; Project administration: Abdul Shakoor, Ramazan Kahraman; Funding acquisition: Ramazan Kahraman, Abdul Shakoor.

Funding

This research was funded by the Qatar National Research Fund (a member of the Qatar Foundation), grant number NPRP13S-0120-200116 and Qatar University internal grant number QUCG-CENG-22/23-461. Statements made herein are solely the responsibility of the authors.

Declaration of Competing Interest

The authors declare no conflict of interest.

Data availability

The raw/processed data required to reproduce these findings cannot be shared at this time due to legal or ethical reasons.

Acknowledgment

The authors would like to thank the Central laboratory Unit (CLU), Qatar University, 2713, Doha, Qatar, for the TEM/EDX analysis facility. Open access funding provided by Qatar National library.

Appendix A. Supplementary data

Supplementary data to this article can be found online at https://doi.org/10.1016/j.clay.2023.106827.

References

Amiri, S., Rahimi, A., 2014. Preparation of supramolecular corrosion-inhibiting nanocontainers for self-protective hybrid nanocomposite coatings. J. Polym. Res. 21 https://doi.org/10.1007/s10965-014-0566-5.
Asadi, N., Naderi, R., Mahdavian, M., 2019. Doping of zinc cations in chemically modified halloysite nanotubes to improve protection function of an epoxy ester coating. Corros. Sci. 151, 69–80. https://doi.org/10.1016/j.corsci.2019.02.022.
Barman, M., Mahmood, S., Augustine, R., Hasan, A., Thomas, S., Ghosal, K., 2020. Natural halloysite nanotubes /chitosan based bio-nanocomposite for delivering norfloxacin, an anti-microbial agent in sustained release manner. Int. J. Biol. Macromol. 162, 1849–1861. https://doi.org/10.1016/j.ijbiomac.2020.08.060.
Chen, X., Hu, D., Zhang, Z., Ma, W., 2019. In situ assembly of halloysite nanotubes@cerium oxide nanohybrid for highly UV-shielding and superhydrophobic coating. J. Alloys Compd. 811, 151986 https://doi.org/10.1016/j.jallcom.2019.151986.
Chen, C., Xiao, G., He, Y., Zhong, F., Li, H., Wu, Y., Chen, J., 2020. Bio-inspired superior barrier self-healing coating: Self-assemble of graphene oxide and polydopamine-coated halloysite nanotubes for enhancing corrosion resistance of waterborne epoxy coating. Prog. Org. Coat. 139, 105402 https://doi.org/10.1016/j.porgcoat.2019.105402.
Deepak, R., Agrawal, Y.K., 2012. Study of nanocomposites with emphasis to halloysite nanotubes. Rev. Adv. Mater. Sci. 32, 149–157.
Ding, R., Zheng, Y., Yu, H., Li, W., Wang, X., Gui, T., 2018. Study of water permeation dynamics and anti-corrosion mechanism of graphene/zinc coatings. J. Alloys Compd. 748, 481–495. https://doi.org/10.1016/j.jallcom.2018.03.160.
Du, M., Guo, B., Jia, D., 2010. Newly emerging applications of halloysite nanotubes: a review. Polym. Int. 59, 574–582. https://doi.org/10.1002/PI.2754.
Dyab, A.K.F., Mohamed, M.A., Meligi, N.M., Mohamed, S.K., 2018. Encapsulation of erythromycin and bacitracin antibiotics into natural sporopollenin microcapsules: antibacterial, cytotoxicity, in vitro and in vivo release studies for enhanced bioavailability. RSC Adv. 8, 33432–33444. https://doi.org/10.1039/C8RA05499A.
Gautam, A., Siva, T., Sathiyanarayanan, S., Gobi, K.V., Subasri, R., 2022. Capped inhibitor-loaded halloysite nanoclay-based self-healing silica coatings for corrosion protection of mild steel. Ceram. Int. https://doi.org/10.1016/j.ceramint.2022.06.288.
Grigoriev, D., Shchukina, E., Shchukin, D.G., 2017. Nanocontainers for Self-Healing Coatings. Adv. Mater. Interfaces 4, 1600318. https://doi.org/10.1002/admi.201600318.
Habib, S., Khan, A., Nawaz, M., Sliem, M.H., Shakoor, R.A., Kahraman, R., Abdullah, A. M., Zekri, A., 2019. Self-healing performance of multifunctional polymeric smart coatings. Polymers (Basel). 11 https://doi.org/10.3390/polym11091519.
Habib, S., Fayyad, E., Nawaz, M., Khan, A., Shakoor, R.A., 2020a. Cerium Dioxide Nanoparticles as Smart Carriers for Self-Healing Coatings Cerium Dioxide Nanoparticles as Smart Carriers for Self-Healing Coatings. https://doi.org/10.3390/nano10040791.
Habib, S., Fayyad, E., Nawaz, M., Khan, A., Shakoor, R.A., Kahraman, R., Abdullah, A., 2020b. Cerium dioxide nanoparticles as smart carriers for self-healing coatings. Nanomaterials 10. https://doi.org/10.3390/nano10040791.
Habib, S., Nawaz, M., Kahraman, R., Ahmed, E.M., Shakoor, R.A., 2022. Effect of the modified hybrid particle on the corrosion inhibition performance of polyolefin based coatings for carbon steel. J. Sci. Adv. Mater. Dev. 7, 100466 https://doi.org/10.1016/j.jsamd.2022.100466.
Heraiz, M., Sahnoune, F., Belhouchet, H., Raghdi, A., Ouali, A., 2017. The kinetics of spinel formation of algerian halloysite by differential thermal analysis. Acta Phys. Pol. A 131, 139–142. https://doi.org/10.12693/APhysPolA.131.139.
Hinton, B.R.W., 2022. Chapter 140 CORROSION PREVENTION AND CONTROL Costofcorrosion Throughout our daily lives, we constantly see the effects o f

environmental degradation. Handb. Phys. Chem. Rare Earths VoL 21 Ed. by K.A. Gschneidner, Jr. L. Eyring Elseuier Sci. B. V, 21, pp. 1–88.
Izadi, M., Shahrabi, T., Mohammadi, I., Ramezanzadeh, B., Fateh, A., 2019. The electrochemical behavior of nanocomposite organic coating based on clay nanotubes filled with green corrosion inhibitor through a vacuum-assisted procedure. Compos. Part B Eng. 171, 96–110. https://doi.org/10.1016/j.compositesb.2019.04.019.
Jana, S., Das, S., Ghosh, C., Maity, A., Pradhan, M., 2015. Halloysite Nanotubes Capturing Isotope Selective Atmospheric CO2. Sci. Rep. 5, 8711. https://doi.org/10.1038/srep08711.
Jia, Y., Qiu, T., Guo, L., Ye, J., He, L., Li, X., 2020. Preparation of pH responsive smart nanocontainer via inclusion of inhibitor in graphene/halloysite nanotubes and its application in intelligent anticorrosion protection. Appl. Surf. Sci. 504, 144496 https://doi.org/10.1016/j.apsusc.2019.144496.
Kamble, R., Ghag, M., Gaikawad, S., Panda, B.K., 2012. Review article halloysite nanotubes and applications: a review. J. Adv. Sci. Res. 3, 25–29.
Kamburova, K., Boshkova, N., Boshkov, N., Atanassova, G., Radeva, T., 2018. Hybrid zinc coatings for corrosion protection of steel using polyelectrolyte nanocontainers loaded with benzotriazole. Coll. Surf. A Physicochem. Eng. Asp. 559, 243–250. https://doi.org/10.1016/j.colsurfa.2018.09.039.
Koch, G., 2017. Cost of corrosion. Trends Oil Gas Corros. Res. Technol. 3–30.
Liu, C., Hou, P., Qian, B., Hu, X., 2022a. Smart healable and reportable anticorrosion coating based on halloysite nanotubes carrying 8-hydroxyquinoline on steel. J. Ind. Eng. Chem. https://doi.org/10.1016/j.jiec.2022.10.050.
Liu, Y., Wang, B., Xie, Y., Chen, Y., Yang, Z., Han, G., Dang, Y., 2022b. A novel dual-responsive halloysite nano-container for anti-corrosion coatings. Anti-Corrosion Methods Mater. 69, 245–252. https://doi.org/10.1108/ACMM-12-2021-2580.
Lun, H., Ouyang, J., Yang, H., 2014. Enhancing dispersion of halloysite nanotubes via chemical modification. Phys. Chem. Miner. 41, 281–288. https://doi.org/10.1007/s00269-013-0646-9.
Montemor, M.F., 2014. Functional and smart coatings for corrosion protection: a review of recent advances. Surf. Coat. Technol. 258, 17–37. https://doi.org/10.1016/J.SURFCOAT.2014.06.031.
Pandey, G., Munguambe, D.M., Tharmavaram, M., Rawtani, D., Agrawal, Y.K., 2017. Halloysite nanotubes - an efficient 'nano-support' for the immobilization of α-amylase. Appl. Clay Sci. 136, 184–191. https://doi.org/10.1016/j.clay.2016.11.034.
Pandey, G., Tharmavaram, M., Khatri, N., Rawtani, D., 2022a. Mesoporous halloysite nanotubes as nano-support system for cationic dyes: an equilibrium, kinetic and thermodynamic study for latent fingerprinting. Microporous Mesoporous Mater. 346, 112288 https://doi.org/10.1016/j.micromeso.2022.112288.
Pandey, G., Tharmavaram, M., Phadke, G., Rawtani, D., Ranjan, M., Sooraj, K.P., 2022b. Silanized halloysite nanotubes as 'nano-platform' for the complexation and removal of Fe (II) and Fe (III) ions from aqueous environment. Sep. Purif. Technol. 293, 121141 https://doi.org/10.1016/j.seppur.2022.121141.
Pasbakhsh, P., Ismail, H., Fauzi, M.N.A., Bakar, A.A., 2010. EPDM/modified halloysite nanocomposites. Appl. Clay Sci. 48, 405–413. https://doi.org/10.1016/j.clay.2010.01.015.
Rawtani, D., Pandey, G., Tharmavaram, M., Pathak, P., Akkireddy, S., Agrawal, Y.K., 2017. Development of a novel 'nanocarrier' system based on Halloysite Nanotubes to overcome the complexation of ciprofloxacin with iron: an in vitro approach. Appl. Clay Sci. 150, 293–302. https://doi.org/10.1016/j.clay.2017.10.002.
Singh, M.K., Agarwal, A., Gopal, R., Swarnkar, R.K., Kotnala, R.K., 2011. Dumbbell shaped nickel nanocrystals synthesized by a laser induced fragmentation method. J. Mater. Chem. 21, 11074–11079. https://doi.org/10.1039/c1jm12320c.
Stankiewicz, A., Szczygieł, I., Szczygieł, B., 2013. Self-healing coatings in anti-corrosion applications. J. Mater. Sci. 48, 8041–8051. https://doi.org/10.1007/s10853-013-7616-y.
Tharmavaram, M., Pandey, G., Rawtani, D., 2018. Surface modified halloysite nanotubes: a flexible interface for biological, environmental and catalytic applications. Adv. Colloid Interf. Sci. 261, 82–101. https://doi.org/10.1016/j.cis.2018.09.001.
Tharmavaram, M., Pandey, G., Bhatt, P., Prajapati, P., Rawtani, D., Sooraj, K.P., Ranjan, M., 2021. Chitosan functionalized Halloysite Nanotubes as a receptive surface for laccase and copper to perform degradation of chlorpyrifos in aqueous environment. Int. J. Biol. Macromol. 191, 1046–1055. https://doi.org/10.1016/j.ijbiomac.2021.09.098.
Tharmavaram, M., Pandey, G., Khatri, N., Rawtani, D., 2023. L-arginine-grafted halloysite nanotubes as a sustainable excipient for antifouling composite coating. Mater. Chem. Phys. 293, 126937 https://doi.org/10.1016/j.matchemphys.2022.126937.
Tonelli, M., Baglioni, P., Ridi, F., 2020. Halloysite nanotubes as nano-carriers of corrosion inhibitors in cement formulations. Materials (Basel). 13, 9–12. https://doi.org/10.3390/ma13143150.
Vijayan, P.P., Hany El-Gawady, Y.M., Al-Maadeed, M.A.S.A., 2016. Halloysite nanotube as multifunctional component in epoxy protective coating. Ind. Eng. Chem. Res. 55, 11186–11192. https://doi.org/10.1021/acs.iecr.6b02736.
Xie, Y., Qian, D., Wu, D., Ma, X., 2011. Magnetic halloysite nanotubes/iron oxide composites for the adsorption of dyes. Chem. Eng. J. 168, 959–963.
Xu, D., Lou, C., Huang, J., Lu, X., Xin, Z., Zhou, C., 2019. Effect of inhibitor-loaded halloysite nanotubes on active corrosion protection of polybenzoxazine coatings on mild steel. Prog. Org. Coat. 134, 126–133. https://doi.org/10.1016/j.porgcoat.2019.04.021.
Yuan, P., Tan, D., Annabi-Bergaya, F., 2015. Properties and applications of halloysite nanotubes: recent research advances and future prospects. Appl. Clay Sci. 112–113, 75–93. https://doi.org/10.1016/J.CLAY.2015.05.001.
Yurdacan, H.M., Murat Sari, M., 2021. Chapter three - Functional green-based nanomaterials towards sustainable carbon capture and sequestration. In: Sari, M.M., Temizel, C., Canbaz, C.H., Saputelli, L.A., Torsæter, O.B.T., S.M. for T. and A.E (Eds.), Advanced Materials and Sensors for the Oil and Gas Industry. Gulf Professional Publishing, pp. 125–177. https://doi.org/10.1016/B978-0-12-824379-4.00004-5.
Zahidah, K.A., Kakooei, S., Ismail, M.C., Bothi Raja, P., 2017. Halloysite nanotubes as nanocontainer for smart coating application: a review. Prog. Org. Coat. 111, 175–185. https://doi.org/10.1016/J.PORGCOAT.2017.05.018.
Zhang, W., Mu, B., Wang, A., 2015. Halloysite nanotubes template-induced fabrication of carbon/manganese dioxide hybrid nanotubes for supercapacitors. Ionics (Kiel). 21, 2329–2336. https://doi.org/10.1007/s11581-015-1412-4.
Zhang, Yanli, Qiang, Y., Ren, H., Cao, J., Cui, L., Zong, Z., Chen, D., Xiang, T., 2022a. Inhibitor loaded functional HNTs modified coatings towards corrosion protection in reinforced concrete environment. Prog. Org. Coat. 170, 106971 https://doi.org/10.1016/j.porgcoat.2022.106971.
Zhang, Yue, Yu, M., Chen, C., Li, S.M., Liu, J.H., 2022b. Self-Healing coatings based on stimuli-responsive release of corrosion inhibitors: a review. Front. Mater. 8, 1–14. https://doi.org/10.3389/fmats.2021.795397.